


# NOISE-OPTIMIZED HOVER PROPELLER DESIGN FOR VTOL CARGO DRONES IN TRANSIENT FLIGHT CONDITIONS

Teresa Moses[1] & Mirko Hornung[1]

[1]Technical University of Munich, Germany

## Abstract

Community noise remains a key barrier to the public acceptance of cargo delivery drones, particularly during hover and transition flight. This paper presents the development of a noise-optimized hover propeller for a lift-and-cruise vertical take-off and landing cargo drone under a performance-critical transient asymmetric inflow condition using a Multidisciplinary Design Optimization (MDO) framework that simultaneously considers aerodynamic and acoustic performance. An analysis of the resulting Pareto-optimal designs identifies the key geometric and aerodynamic mechanisms responsible for lower farfield noise emissions. The results show a noise reduction potential exceeding 5 dB(A), with reduced rotational speed emerging as the primary characteristic of the low-noise designs. Adaptations of the chord and twist distributions enable the required thrust to be maintained at lower rotational speed through increased blade area and sectional lift coefficients, while the resulting increase in torque and motor current ultimately limits further noise reduction. Despite increased aerodynamic loading, reductions in both thickness and loading noise are achieved. Validation against higher-fidelity unsteady Computational Fluid Dynamics shows good agreement in integral aerodynamic performance, dominant tonal components, and principal directivity characteristics, while revealing an underprediction of approximately 5 dB(A) in the maximum A-weighted level, primarily due to differences in higher-frequency harmonic content.

**Keywords:** Unmanned Aerial System, Hover Propeller, Noise Optimization, Computational Aeroacoustics, Transient Flight

## 1. Introduction

Recent surveys [1] indicate that the public is generally receptive to cargo delivery drones, particularly for emergency applications, but concerns about increased community noise remain. A primary mitigation strategy is to reduce noise at its dominant source, implying the adjustment of the propeller geometry to minimize its noise generation. Multidisciplinary Design Optimization (MDO) provides an effective framework for this task [2, 3]. Unlike traditional methods that focus on a single property, such as efficiency, MDOs provide the possibility of considering multiple constraints when identifying an optimal propeller design. By parametrizing the airfoil geometry, blade shape parameters and overall propeller characteristics, MDOs can iteratively find new propeller geometries that account for both aerodynamic performance and acoustic emissions simultaneously [3]. Moreover, multiple and even conflicting operating points can be included as constraints to achieve an optimal trade-off design. E.g., [2] designed a dual-mode propeller optimized for cruise, while treating hover as an additional constraint. The final design demonstrated a significant reduction in the maximum A-weighted sound pressure level ($L_{\mathrm{A,max}}$) of approximately 7 dBA during cruise, at the cost of a 5% efficiency penalty, while still maintaining adequate hover capability.

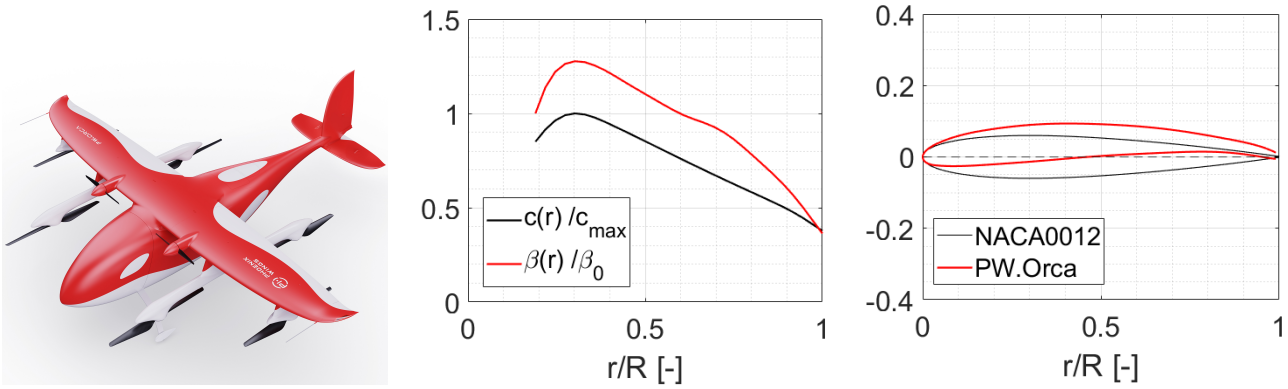
Since drones operate in close proximity to the public during hover and transition, these operating conditions are particularly critical with respect to community noise emissions. Consequently, optimizing hover propellers to minimize their acoustic signature is of major importance. As stated by [4],

propellers intended for Urban Air Mobility applications must function in complex, highly interactive flow environments that differ significantly from axial inflow conditions typically assumed in propeller design. Their study examined the aerodynamic loading of propellers under asymmetric inflow conditions and showed that increasing the inflow velocity angle leads to larger blade-loading oscillations. These enhanced unsteady loads, in turn, amplify the magnitudes of blade passing frequency (BPF) and its harmonics.

In this context, the Technical University of Munich is developing a noise-optimized hover propeller for the vertical take-off and landing (VTOL) cargo drone 'PW.Orca' of German manufacturer Phoenix-Wings GmbH [5]. Based on the MDO framework of [2], the propeller blade geometry is optimized for a performance-critical transient flight condition, yielding a Pareto front that captures the trade-off between total performance efficiency and noise emissions. From this design space, representative configurations are selected to identify key noise-reduction mechanisms. The results for the minimum-noise propeller obtained from the MDO approach are further compared to the results generated via Computational Fluid Dynamics (CFD), employing a hybrid acoustic analogy approach that couples an Unsteady Reynolds-Averaged Navier Stokes (URANS) solver with a Ffowcs Williams–Hawkings (FW-H) acoustic solver [6]. The key contribution of this work is the systematic investigation of geometric propeller noise mitigation mechanisms for a transient flight condition, which has received limited attention in previous studies.

## 2. Methods

The PW.Orca [5] displayed in Figure 1a is a separate lift-and-cruise cargo drone equipped with 2 cruise and 6 hover propellers. Its wingspan and maximum takeoff weight are 2.98 m 52 kg, respectively. The baseline hover propeller utilized for these investigations is a 2-bladed, fixed-pitch 29 in propeller with a maximum chord $c_{max}$ = 0.0666 m and root (r/R = 0.2) twist angle $\beta_0$ = 14.5°. The respective chord and twist distributions are displayed in Figure 1b over the non-dimensional radial position, with $r$ and $R$ being the local and total propeller radius. The blade utilizes a radially constant airfoil cross-section, shown in Figure 1c with a NACA 0012 profile included for reference.




(a) PW.Orca. (b) Chord and twist distribution. (c) Airfoil.

Figure 1 – Lift-and-cruise VTOL cargo drone PW.Orca (image courtesy of Phoenix-Wings GmbH) and its baseline hover propeller characteristics.

With the underlying goal of improving the noise signature of the PW.Orca during noise-critical mission segments, the fixed-pitch hover-propeller geometry is optimized using the MDO framework by [2]. Its general workflow is described next.

### 2.1 Basics Regarding the Optimization Workflow

The objective is to identify a propeller design that achieves an optimal trade-off between low noise emissions and high efficiency at a specified operating point within a predefined design space. The optimization problem is formulated as a constrained multi-objective optimization, where noise is minimized while satisfying performance and feasibility constraints.

To ensure a physically meaningful and computationally manageable design space, geometric and operational constraints are imposed. Firstly, the design variables and their permissible ranges need

to be defined. These include airfoil contour parameters as well as blade and propeller shape parameters such as chord, twist, or the number of blades. Further, a target operating point is specified by the freestream inflow conditions, a required thrust level, and electric motor characteristics and limitations. To promote robust performance beyond the design condition, additional operating points can be introduced as constraints. These ensure feasibility across a range of operating conditions and enforce trade-offs between competing objectives, such as cruise and hover performance. Additionally, the observer locations used for the acoustic evaluation must be defined.

The optimization is implemented as an iterative stochastic selection search. First, an initial population of propeller geometries is generated to explore the design space. Successfully evaluated designs are used to identify an initial Pareto front, representing the best trade-off solutions between total efficiency $\eta_{tot}$ and selected noise metric, e.g. $L_{\mathrm{A,max}}$. This implies that designs on the Pareto front are not simultaneously outperformed by another design in both objectives; improving one objective would therefore require sacrificing performance in the other. Subsequently, new candidate geometries are generated by perturbing the current Pareto-optimal designs. The resulting designs are re-evaluated and the Pareto front is updated iteratively. Notably, the perturbation size is progressively reduced over the course of the optimization, shifting the search from broader exploration towards local refinement. The procedure is repeated until the prescribed number of iterations is reached, ultimately yielding a set of Pareto-optimal propeller designs. Note that the total efficiency accounts for aerodynamic, motor and electronic speed controller efficiencies.

The aerodynamic design evaluation is performed using the in-house developed Synthesis and Analysis Rotor Framework (SARF) presented by [7], a propeller performance calculation tool that is based on the Blade Element and Momentum Theory (BEMT). In addition to axial inflow conditions, SARF enables the analysis of oblique inflow scenarios and accounts for tip losses via the Prandtl tip loss factor [8]. Following classical BEMT, the blade geometry is discretized radially, while the analysis is extended across a full rotor revolution using a discrete circumferential resolution to capture the time-varying aerodynamic loading. In an iterative process, sectional aerodynamic quantities such as lift and drag forces, inflow angle, and induced velocity are determined. The required aerodynamic coefficients are obtained from precomputed airfoil databases spanning a range of Mach and Reynolds numbers, thereby accounting for variations in polar characteristics under different local flow conditions. This finally yields the integrated propeller performance, including, but not limited to, thrust, torque, and aerodynamic efficiency. Within the optimization loop, SARF is iteratively executed for each candidate design to determine the rotational speed required to meet the prescribed target thrust at all specified operating points (target and constraint conditions). Subsequently, the capability of the motor to supply the required output power is assessed, and infeasible designs are discarded. The remaining feasible designs are then evaluated acoustically.

The acoustic computations are focused on tonal noise and are performed using the state-of-the-art acoustic solver PSU-WOPWOP [9], which is fully integrated into the optimization loop. The solver implements the F1A formulation [10] of the FW-H equation [11], whereby the far-field sound pressure is decomposed into thickness and loading noise contributions. Thickness noise is computed from the blade surface geometry, requiring the node coordinates and surface normals of the discretized blade mesh. For the loading noise, PSU-WOPWOP supports the use of spanwise line force vectors instead of surface pressure distributions. This reduces the original surface integrals to computationally less expensive line integrals along the blade span. For obtaining these line forces, differential lift ($dL$) and drag ($dD$) forces acting on a blade element must be computed from

$$dL = \frac{\rho}{2} v_{\mathrm{rel}}^2 \, c \, C_L \ , \tag{1}$$

$$dD = \frac{\rho}{2} v_{\mathrm{rel}}^2 \, c \, C_D \ , \tag{2}$$

where $\rho$ is the density, $c$ the local chord length, $v_{\mathrm{rel}}$ the local inflow velocity, and $C_L$ and $C_D$ are the sectional lift and drag coefficients.

To also account for asymmetric inflow conditions, the original formulation of $v_{\mathrm{rel}}$ assuming solely axial inflow is herein extended by including the tangential component of the freestream velocity $U_\infty$, which

changes over one rotation depending on the azimuthal blade position $\psi$. The resulting axial and tangential velocity components, $u_{\mathrm{ax}}$ and $u_{\mathrm{tan}}$, at a blade element can then be expressed as:

$$u_{\mathrm{ax}} = U_{\infty} \cos \alpha_{\infty} \ , \tag{3}$$

$$u_{\mathrm{tan}} = U_{\infty} \sin \alpha_{\infty} \sin \psi + \Omega r \ . \tag{4}$$

$\alpha_{\infty}$ denotes the freestream inflow angle, and $\Omega r$ the tangential velocity induced by rotor rotation. Following [7], $v_{\mathrm{rel}}$ results in

$$v_{\mathrm{rel}} = \sqrt{u_{\mathrm{ax}}^2 + u_{\mathrm{tan}}^2 - v_{\mathrm{ind}}^2} \ , \tag{5}$$

where $v_{\mathrm{ind}}$ is the local induced velocity. Notably, the velocity decomposition assumes a planar inflow representation and does not include a freestream velocity component perpendicular to this plane.

## 2.2 Case-specific Propeller Optimization Setup

In the present study, the optimization is restricted to blade shape parameters, while the airfoil geometry is not optimized but adopted from the baseline propeller (see Figure 1c) and kept constant along the radius. Neglecting blade sweep entirely, the main design variables reduce to radius, chord, and twist. Due to the fixed installation position of the hover propellers on the vehicle, the propeller radius is restricted to a maximum increase of 5% relative to the baseline design. Since the hover propellers are inactive during cruise and aligned with the flight direction to minimize parasitic drag, the number of blades is fixed at two. Powertrain limitations are taken into account by imposing a maximum allowable electric current of 60 A, thereby constraining the feasible operating conditions.
The selected acoustic objective for the optimization is the $L_{A,\mathrm{max}}$. To evaluate the far-field noise emissions of the candidate designs, eight receiver locations are defined on a circular arc with a radius of 30 m around the rotor center in a plane perpendicular to the rotor disk. The receivers are located upstream of the rotor, where pronounced acoustic radiation is anticipated under oblique inflow conditions [12, 13]. The receivers are evenly distributed over an angular range spanning from 10° above to 30° below the rotor plane, as sketched in Figure 2.

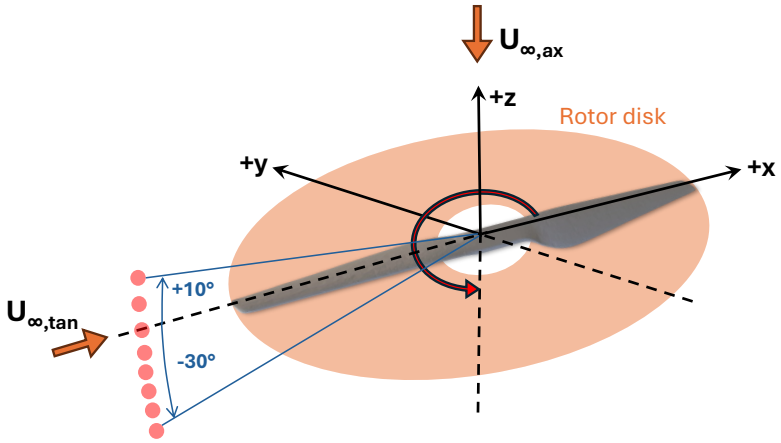



Figure 2 – Schematic of the propeller geometry, coordinate system definition, receiver placement (red dots), and freestream inflow definition set for the optimization. $U_{\infty,ax}$ and $U_{\infty,tan}$ designate axial and tangential freestream inflow velocities.

With the aim to achieve a meaningful noise reduction where it matters most while maintaining robust performance across all flight states, a performance-critical flight condition was selected as target operating point. It corresponds to a 45° climb at 4.24 m/s with a thrust requirement of 100 N. This condition represents a transient flight phase in which the drone operates close to the public, making noise emissions particularly relevant. Furthermore, the 45° climb constitutes a thrust-demanding operating point, ensuring that the optimized propeller meets aerodynamic requirements under high loading conditions. Additionally, a static thrust condition of 150 N is included as a secondary constraint to ensure adequate hover performance. Atmospheric conditions correspond to the ISA standard atmosphere [14] at 500 m above sea level.

Without imposing explicit efficiency or noise constraints, the MDO tool systematically explores the design space by varying the adjustable design parameters and ultimately outputs all feasible propeller designs along with their key geometric, aerodynamic, propulsive, and acoustic performance parameters. This allows a direct comparison of most efficient and least noise-polluting designs.

## 2.3 Result Verification via CFD

To verify the aerodynamic and acoustic predictions obtained from the optimization framework, a higher-fidelity CFD simulation of the minimum-noise design is performed under identical operating conditions. A hybrid acoustic analogy approach is employed, in which the unsteady flow field is resolved using URANS and the resulting aerodynamic solution is subsequently used as input to an acoustic solver based on the FW-H acoustic analogy [11].

The CFD simulation is conducted using Simcenter STAR-CCM+. The computational domain consists of a stationary spherical freestream region with a radius of $50R$ and a rotating cylindrical region enclosing the propeller, with a radius of $1.08R$ and a thickness of $0.3R$. The computational mesh comprises approximately 12.6 million cells, with local refinement around the blade geometry and within the wake region. Propeller motion is represented by rigid-body rotation of the inner region. Turbulence is modeled using the Shear Stress Transport (SST) model in combination with an All-$y^+$ wall treatment. An implicit coupled solver with second-order spatial and temporal discretization is employed using a physical time step of $1 \times 10^{-4}$ s and eight inner iterations per time step. In total, nine rotor revolutions are simulated, corresponding to a physical time of 0.1723 s. The first four revolutions are used to establish a periodic flow field, while the final five revolutions are used for the acoustic evaluation. The general numerical setup and mesh strategy are based on the methodology described for a full-vehicle simulation in [6] and are adapted here to the isolated-propeller configuration.

The software-integrated acoustic solver employs the Farassat 1A formulation [10]. Notably, broadband noise contributions are not explicitly resolved, as the applied URANS approach does not resolve the turbulent flow structures responsible for their generation. The acoustic pressure is evaluated using a spherical array of 222 receivers uniformly distributed at a radius of 30 m from the propeller center. This provides full angular coverage of the radiated sound field, enabling the analysis of tonal spectra, directivity patterns, and overall sound pressure levels. Figure 3 illustrates the lower receiver hemisphere and the adopted azimuth ($\Psi$) and elevation ($\Phi$) angle conventions.

For consistency, an identical receiver sphere is reconstructed from the optimizer results. The resulting aerodynamic and acoustic predictions are then compared to quantify the deviations between the BEMT-based optimization framework and the higher-fidelity CFD solution.

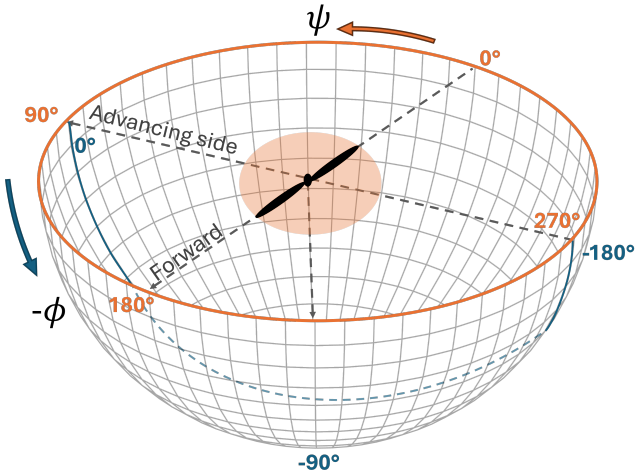
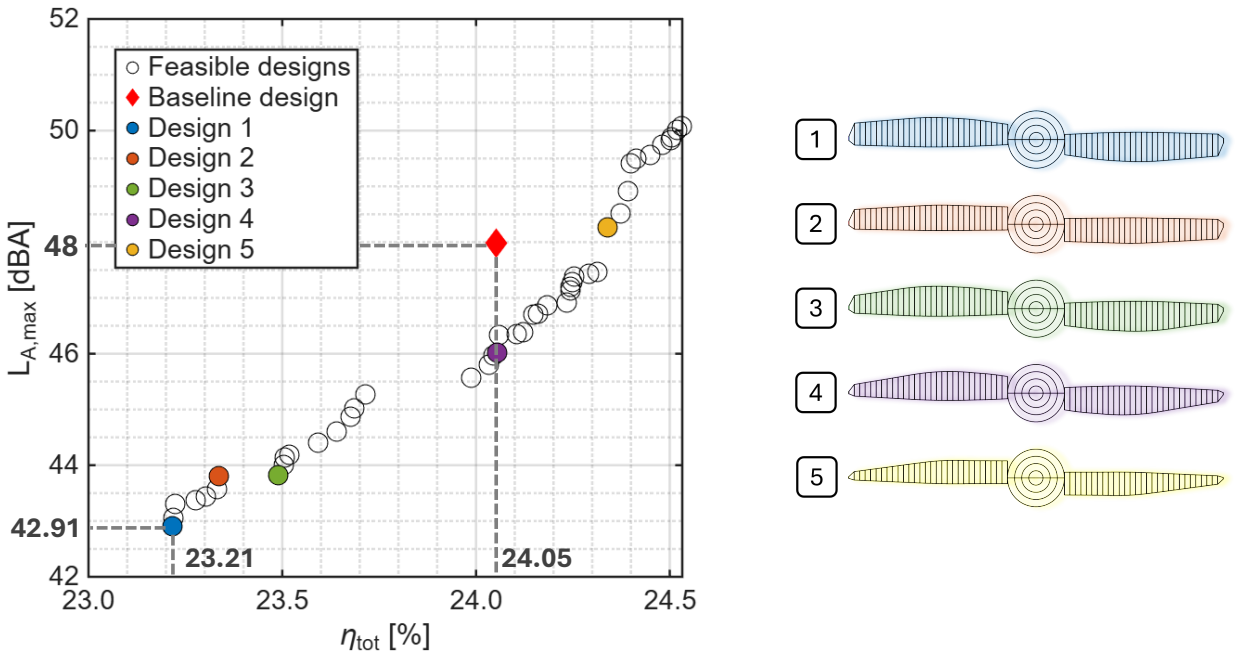



Figure 3 – Schematic of the lower receiver hemisphere illustrating the adopted convention for the azimuth angle $\Psi$ and elevation angle $\Phi$.

## 3. Results

Figure 4a presents the Pareto front obtained for the 45° climb condition, showing the optimal trade-off solutions between $L_{A,max}$ and the total efficiency $\eta_{tot}$. The results indicate a noise reduction potential exceeding 5 dBA with a 3.5% sacrifice in $\eta_{tot}$ relative to the baseline design. To identify the optimizer's strategy for low-noise or high-efficiency propeller designs, five representative configurations along the Pareto front are selected for further analysis. Design 1 provides the highest noise reduction potential. Designs 2 and 3 exhibit nearly identical $L_{A,max}$ levels, while the latter operates at a slightly higher $\eta_{tot}$. A similar comparison can be conducted between the baseline and Design 5, which achieves approximately the same $L_{A,max}$ as the baseline design while providing a 1.2% increase in efficiency. Finally, Design 4 is selected because it shows the same $\eta_{tot}$ as the baseline configuration while reducing $L_{A,max}$ by 2 dBA.

Figure 4b presents top views of the selected propeller geometries, providing a first qualitative impression of the geometric variations along the Pareto front. While the radius of all optimized designs remains within ±1% of the baseline propeller radius, substantial differences in chord distributions can already be observed. Notably, care must be taken when interpreting these representations, as a stronger blade twist distribution can distort the apparent blade geometry. Nevertheless, a general trend of increasing blade area with decreasing $L_{A,max}$ can be observed. For a quantitative analysis, the selected designs are next compared and examined in terms of their integral performance parameters, providing a deeper insight into differences in thrust capability, power requirements, and efficiency.




(a) Pareto front displaying the trade-off between total efficiency $\eta_{tot}$ and maximum sound pressure level $L_{A,max}$.

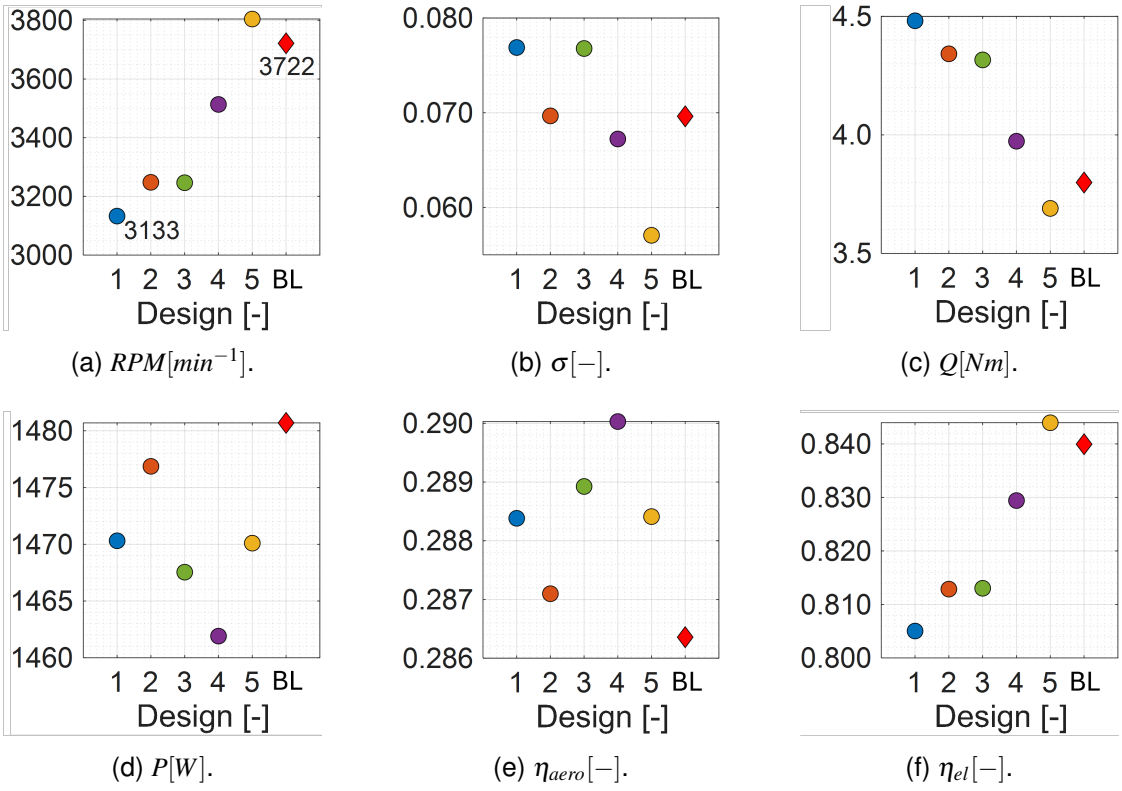
(b) Top view of selected designs from the Pareto front.

Figure 4 – Pareto front of feasible propeller designs optimized for a 45° climb at 4.24 m/s and target thrust of 100 N, highlighting the selected designs chosen for further analysis.

### 3.1 Integral Performance Parameters

Figure 5 summarizes the characteristic performance parameters of the selected Pareto-optimized designs relative to the baseline propeller. As shown in Figure 5a, rotational speed $RPM$ decreases consistently toward the low-noise end of the Pareto front, with Design 1 operating 589 $\mathrm{min}^{-1}$ below the baseline. This clear correlation already identifies reduced $RPM$ as a key characteristic of the low-noise designs. Physically, lower $RPM$ reduces the blade tip velocity, which is a well-established mechanism for reducing propeller noise emissions [15, 16]. Since all designs are constrained to generate the same target thrust of 100 N, operation at lower $RPM$ requires increased aerodynamic loading. As a first indication of how the optimizer accommodates this requirement, Figure 5b shows a

tendency of increasing solidity $\sigma$ for the low-noise designs. The additional blade area associated with higher $\sigma$ contributes to maintaining the required thrust at reduced rotational speed. Notably, Design 2 achieves the second-lowest noise level while exhibiting approximately the same $\sigma$ as the baseline. This points toward the important role of detailed radial blade geometry and sectional operating conditions in enabling operation at reduced $RPM$.




(a) $RPM[min^{-1}]$. (b) $\sigma[-]$. (c) $Q[Nm]$.

(d) $P[W]$. (e) $\eta_{aero}[-]$. (f) $\eta_{el}[-]$.

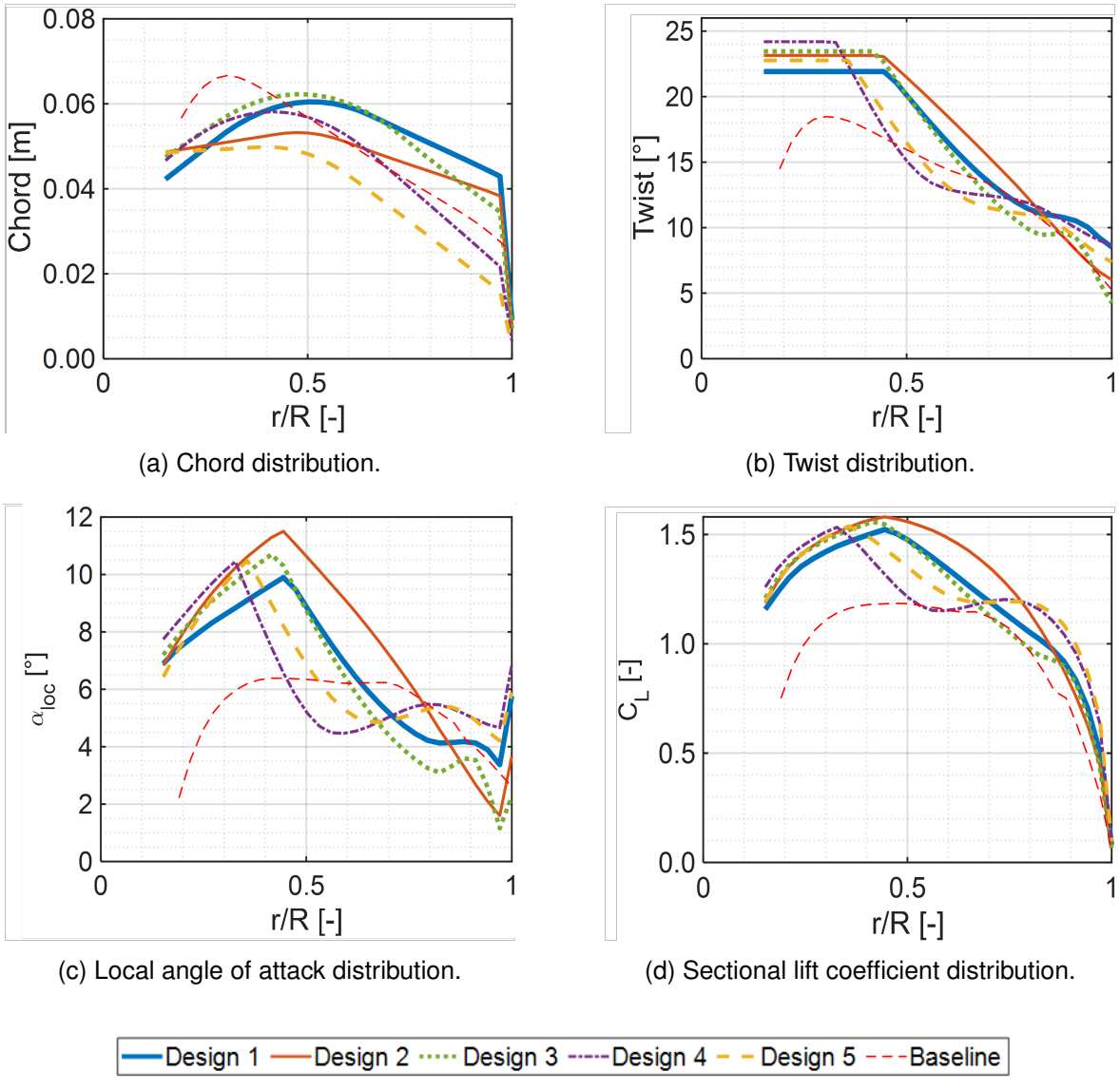
Figure 5 – Performance parameters of Pareto-optimized and baseline (BL) propeller designs.

As shown in Figure 5c, the lower $RPM$ is accompanied by an increase in torque $Q$. However, higher torque does not imply higher mechanical power $P$, since the latter depends on both torque and rotational speed. Figure 5d demonstrates that the increase in torque is largely compensated by the simultaneous reduction in $RPM$, resulting in only small differences in $P$ between the investigated designs. In fact, the minimum-noise Design 1 requires slightly less mechanical power than the baseline. This is also reflected in the aerodynamic efficiency $\eta_{aero}$, presented in Figure 5e. All Pareto-optimized designs exhibit a higher $\eta_{aero}$ than the baseline, while the differences between the designs remain small. The relatively low absolute values result from the low-advance-ratio operating condition ($J \approx 0.1$), where induced-flow effects dominate. Furthermore, no clear relationship between $\eta_{aero}$ and $L_{A,max}$ is observed. E.g., Designs 1 and 5 have nearly identical $\eta_{aero}$ despite being at opposite locations along the Pareto front (Figure 4a). This demonstrates that $\eta_{aero}$ is not the primary parameter governing the noise-efficiency trade-off.

Instead, the electrical efficiency $\eta_{el}$ in Figure 5f exhibits a strong relationship with the position along the Pareto front. The combination of lower rotational speed and higher torque shifts the electric motor to a less favorable operating condition, resulting in decreasing $\eta_{el}$ toward the low-noise designs. This effect is also reflected in the motor current: Design 1 reaches the imposed current limit of 60 A, whereas Design 5 requires 50 A. Since motor torque is approximately proportional to current, its limitation ultimately constrains further reductions in $RPM$ and, consequently, the achievable acoustic benefit. The geometric and sectional mechanisms enabling the low-$RPM$ operating strategy are examined in the following.

## 3.2 Geometric and Aerodynamic Mechanisms

Figures 6a and 6b show the chord and twist distributions of the selected blade designs. The chord distribution determines the available lifting area along the blade span, while the twist contributes to setting the local aerodynamic operating conditions. All optimized designs shift the maximum chord $c_{max}$ from the inner blade region toward the mid-span, with Designs 1-3 reaching $c_{max}$ near $0.5R$. This results in a more elliptical chord distribution and increases the load-carrying capability of the mid-span sections [17]. Toward the outer span, the efficiency-oriented designs exhibit strong chord taper, whereas the low-noise designs retain larger chord values. This trend is most pronounced for Design 1. The resulting increase in blade area, consistent with the higher $\sigma$ identified in Section 3.1, provides the additional lifting area for generating the required thrust at reduced $RPM$.




(a) Chord distribution.

(b) Twist distribution.

(c) Local angle of attack distribution.

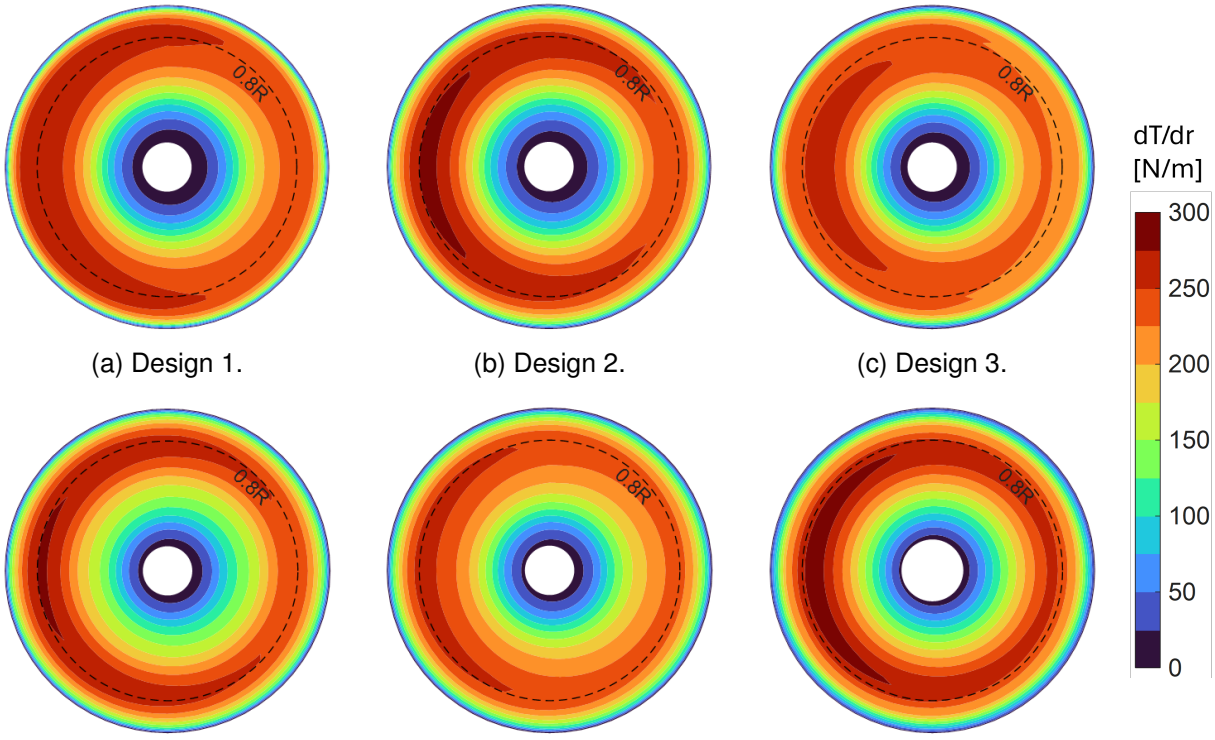
(d) Sectional lift coefficient distribution.

Figure 6 – Blade geometry parameters and mean lift coefficient $C_L$ and local angle of attack $\alpha_{loc}$ for one rotation along the non-dimensional radius for the Pareto-optimized and baseline blade designs.

The twist distributions of the optimized designs also differ significantly from the baseline. They exhibit higher twist values close to the hub, while farther outboard all designs except Design 2 follow a distinctly non-linear behavior. Design 2 exhibits a linear decrease in twist over most of the blade span. A non-linear twist distribution is therefore neither unique to nor required for low-noise operation, indicating that different twist distributions can establish the sectional operating conditions required by the respective designs.

The aerodynamic consequences of these geometric modifications are reflected in the radial distri-

butions of the local angle of attack $\alpha_{\text{loc}}$ and sectional lift coefficient $C_L$ shown in Figures 6c and 6d. Despite the asymmetric inflow condition, the azimuthal variations of these quantities remain small. Thus, the graphs represent the average distributions over one rotor revolution. The baseline exhibits a uniform $\alpha_{loc}$ and $C_L$ over much of the mid-span, with $C_L \approx 1.1$–$1.2$. In contrast, the optimized designs reach higher $\alpha_{loc}$ in the inner-to-mid-span region and higher $C_L$ nearly across the entire span with maximum $C_L \approx 1.5$. This demonstrates that the aerodynamic adaptation to low-$RPM$ operation is achieved through both the available lifting area and high sectional lift coefficients. Notably, toward the outer span, the interaction of $C_L$ with the chord length becomes particularly apparent: designs with stronger chord taper maintain comparatively high $C_L$, allowing a high sectional loading to be maintained despite the reduced lifting area. In contrast, Design 1 retains a larger chord and can generate outer-span forces over a larger lifting area without requiring correspondingly high $C_L$.
A qualitatively similar radial behavior of $\alpha_{\text{loc}}$ and $C_L$ is observed at the constrained 150 N static-thrust operating point (not shown), although their absolute magnitudes differ. This similarity is consistent with the low advance ratio of the transient-flight design condition ($J \approx 0.1$), for which the sectional flow remains strongly dominated by the rotational and induced velocity components. The investigated 45° climb condition therefore remains comparatively hover-like in terms of its mean radial aerodynamic behavior. The oblique freestream primarily introduces an additional azimuthal variation in blade loading, which becomes apparent in the rotor-disk distributions of the sectional thrust loading $dT/dr$ presented in Figure 7.




(a) Design 1. (b) Design 2. (c) Design 3.

(d) Design 4. (e) Design 5. (f) Baseline.

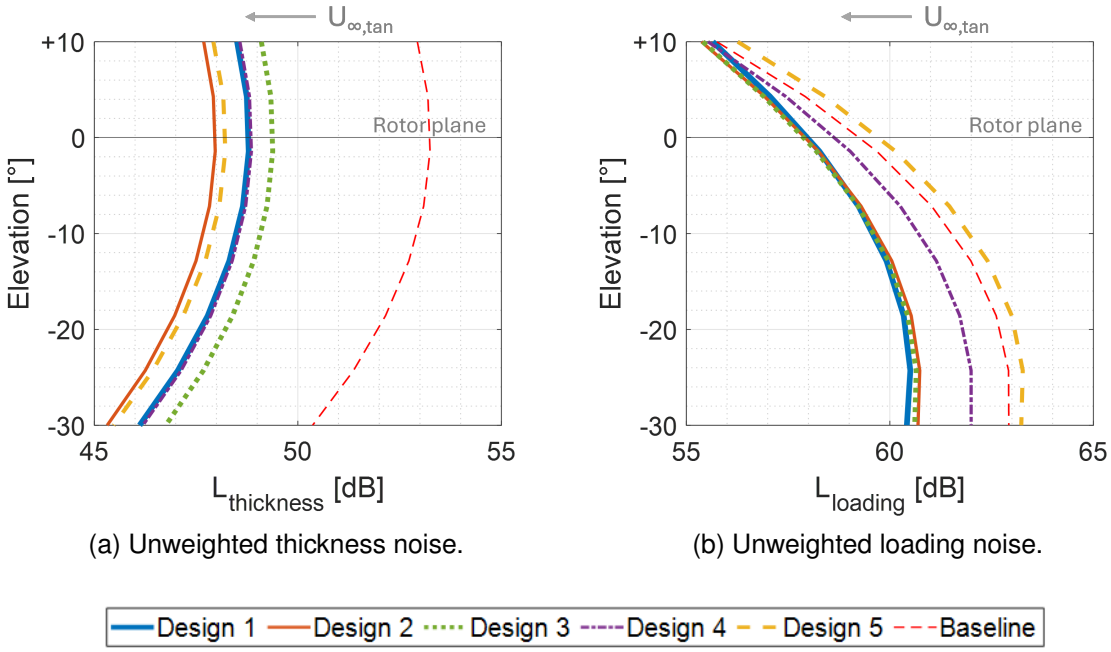
Figure 7 – Sectional loading $dT/dr$ over the rotor disk for baseline and Pareto-optimized designs (propellers rotate counterclockwise; $U_{\infty,tan}$ from the bottom).

Focusing on the general radial trend, all designs exhibit low sectional thrust generation inboard, followed by increasing $dT/dr$ toward the mid-to-outer span and unloading at the blade tip. However, the radial position and magnitude of maximum loading differ between designs. While the baseline (Figure 7f) concentrates its highest sectional loading at radial positions below $0.8R$, Design 1 (Figure 7a) maintains high loading over a broader outer-span region and carries substantial loading farther outward than any other configuration.
Superimposed on this radial loading distribution is the azimuthal variation introduced by the oblique inflow, with the highest $dT/dr$ occurring on the advancing side of the rotor disk. The resulting cyclic

variation in integrated blade thrust ranges from approximately 7.4% to 8.5% of the corresponding mean blade thrust. Interestingly, Design 1 exhibits the largest variation, although the differences between the designs are minor. This observation is nevertheless noteworthy in combination with its pronounced outer-span loading: the minimum-noise configuration neither unloads the outer blade region nor exhibits reduced cyclic thrust variations, which are mechanisms expected to generally reduce acoustic emissions [18, 19]. This indicates that the acoustic benefit of Design 1 cannot be attributed to conventional aerodynamic unloading or reduced cyclic load variations. Instead, this counterintuitive combination motivates a closer examination of the resulting acoustic characteristics and, in particular, the role of rotational speed in the following section.

### 3.3 Acoustic Performance of Noise-optimized vs. Baseline Designs

To assess the underlying acoustic source mechanisms independently of frequency weighting, the following analysis first considers unweighted sound pressure levels, while A-weighted levels are evaluated later for comparison with the acoustic optimization objective. To identify how acoustic reductions are achieved, the tonal noise is separated into its thickness- and loading-noise contributions. Figure 8 presents both components at the eight receiver locations defined in Section 2.2. Recalling Figure 2, the receivers are positioned in a plane perpendicular to the rotor disk in upstream direction.




(a) Unweighted thickness noise.

(b) Unweighted loading noise.

Figure 8 – Acoustic noise emissions at the receiver locations used during the optimization. The tangential component of the freestream inflow velocity $U_{\infty,\tan}$ is directed from the right to the left.

Figure 8a shows that thickness noise $L_{\text{thickness}}$ reaches its maximum close to the rotor plane, with the baseline producing substantially higher levels than all optimized designs. Thickness noise originates from the displacement of the surrounding fluid by the moving blade and therefore depends on both blade kinematics and blade volume [20]. The reduced rotational speeds of the low-noise designs decrease the local blade velocities and contribute to the observed reduction. However, $RPM$ alone does not explain the ranking among the optimized configurations. Most notably, Design 5 operates at the highest rotational speed while exhibiting the second-lowest $L_{\text{thickness}}$ levels, whereas Design 1 operates at the lowest rotational speed but does not yield the minimum thickness-noise contribution. This demonstrates the additional influence of blade geometry: Design 5 combines low solidity with strong chord taper toward the outer span, reducing blade volume in regions of high tangential velocity. Conversely, the low-noise designs retain larger chord values farther outboard, which can partially counteract the acoustic benefit of their reduced rotational speed. Design 2 appears to provide the most favorable combination of both effects: it operates at substantially reduced $RPM$ while retaining a solidity comparable to the baseline, resulting in the lowest $L_{\text{thickness}}$ levels.

For loading noise $L_{\text{loading}}$, the reduction in $RPM$ competes with the increased aerodynamic loading required to maintain the prescribed thrust. While the increased aerodynamic loading would be expected to also increase the acoustic source strength, reducing $RPM$ increases the timescale over which the rotating force field varies relative to a stationary observer. Figure 8b supports this interpretation: despite its pronounced outer-span loading, Design 1 exhibits the lowest loading-noise levels, while $L_{\text{loading}}$ generally increases with $RPM$ across the optimized designs. Thus, the minimum loading noise is not achieved by unloading the blade, but by enabling the required thrust to be generated at substantially lower rotational speed.

In addition to this magnitude trend, $L_{\text{loading}}$ exhibits a pronounced asymmetric directivity, with maximum levels below the rotor plane. Under purely axial inflow, the aerodynamic loading is approximately invariant with blade azimuth. Within the considered elevation plane, the resulting loading-noise directivity would be approximately symmetric across the propeller plane and the highest levels would be expected within the propeller plane [13]. Under oblique inflow, however, the aerodynamic conditions vary with blade azimuth, resulting in periodic variations of the blade loading over one revolution. Consequently, the loading-noise radiation becomes asymmetric and the dominant radiation lobe is displaced below the propeller plane. Goyal et al. [13] similarly identified the azimuthal variation of blade loading as the primary mechanism responsible for changes in noise directivity at nonzero inflow angles. The similar directivity across the optimized designs therefore suggests that the optimization primarily changes the loading-noise magnitude while retaining the characteristic asymmetry imposed by the oblique inflow.

Comparing the two source mechanisms, the reduction relative to the baseline is more pronounced for thickness noise than for loading noise. While both benefit from reduced rotational speed, the loading-noise reduction is partly offset by the increased aerodynamic forces required to maintain thrust. Thickness noise is not subject to this opposing aerodynamic effect. Nevertheless, loading noise remains the dominant contribution, with maximum levels of approximately 60–63 dB compared with 48–53 dB for thickness noise. Consequently, the stronger reduction in thickness noise has a comparatively limited effect on the total tonal-noise level.

Overall, the optimization demonstrates that substantial noise reductions can be achieved by enabling operation at significantly reduced rotational speed. Through adaptations of the blade geometry and sectional operating conditions, the optimizer identifies designs that maintain the prescribed thrust at lower $RPM$. Despite the associated increase in aerodynamic loading and the periodic variations in blade loading introduced by the 45° inflow angle, reductions in both thickness and loading noise are achieved. Further exploitation of this low-$RPM$ strategy is ultimately constrained by the motor operating limits. As Design 1 represents the minimum-noise configuration within the investigated design space, it is selected for the subsequent CFD-based validation of the BEMT-based optimization approach.

## 3.4 Validation of Optimization Results with CFD Data

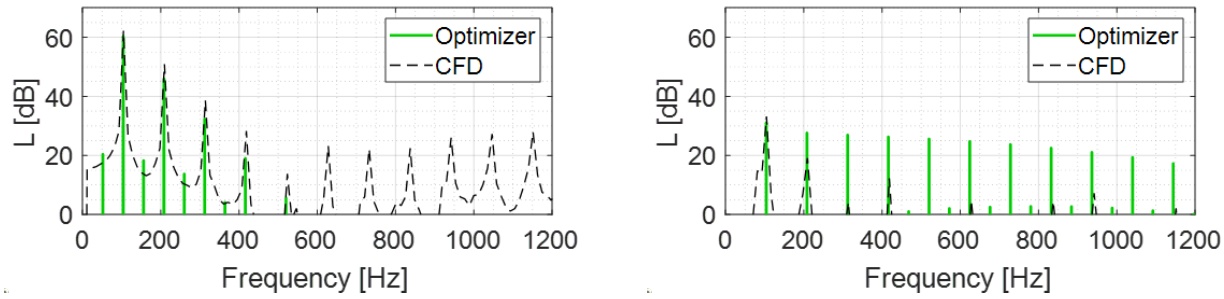
The BEMT-based optimization framework relies on a reduced-order representation of the propeller aerodynamics, enabling the evaluation of a large number of designs at comparatively low computational cost. Generating the complete acoustic receiver sphere for a single propeller design requires approximately 0.3 CPU h. To assess the validity of the resulting predictions, the minimum-noise design is additionally evaluated using higher-fidelity CFD. In contrast to the BEMT formulation, CFD resolves the three-dimensional, time-dependent flow field and therefore provides an independent numerical reference for assessing the simplified optimization framework, however, at a substantially higher computational cost of approximately 1255 CPU h. The comparison is performed at three levels: integral aerodynamic performance, tonal spectral characteristics and directivity, and the resulting A-weighted noise levels.

Table 1 summarizes the differences in average thrust, torque and $\eta_{aero}$ predicted by the optimizer and CFD. Overall, both methods show good agreement, with CFD predicting slightly lower thrust (-2.4%), higher torque (+4.9%), and consequently lower $\eta_{aero}$ (-7.3%). These deviations are consistent with the higher-fidelity representation of three-dimensional and unsteady flow phenomena in CFD that are nor resolved within the BEMT formulation [21].

Table 1 – Average aerodynamic parameters for the noise-optimized design derived by the optimizer versus the CFD simulation.

| **Method** | **Mean Thrust [N]** | **Mean Torque [Nm]** | **Mean $\eta_{aero}$** |
|---|---|---|---|
| Optimizer | 100.00 | 4.48 | 0.288 |
| CFD URANS | 97.06 | 4.70 | 0.267 |

Beyond the integral aerodynamic quantities, Figure 9 compares the tonal spectra predicted by the optimizer and CFD for the forward ($\Psi = 180°$, $\Phi = 0°$) and downward ($\Phi = -90°$) emission directions. In both directions, distinct peaks occur at the blade-passing frequency (BPF) of 104 Hz and its harmonics, demonstrating that the BEMT-based framework reproduces the dominant tonal structure obtained from CFD. The amplitude of the fundamental BPF agrees within approximately 2 dB for both observer directions. Differences become more pronounced at higher harmonics and depend on the observer direction. In the forward direction, both methods exhibit a similar decay of the dominant harmonics up to approximately $5 \cdot \mathrm{BPF}$, while CFD predicts additional high-frequency harmonic content beyond this range. In the downward direction, the optimizer predicts higher amplitudes for several higher-order harmonics. Since the thickness-noise contribution approaches zero along the propeller axis, these differences are predominantly associated with the loading-noise contribution.




(a) Forward emission direction ($\Psi = 180°$)

(b) Downward emission direction ($\Phi = -90°$)

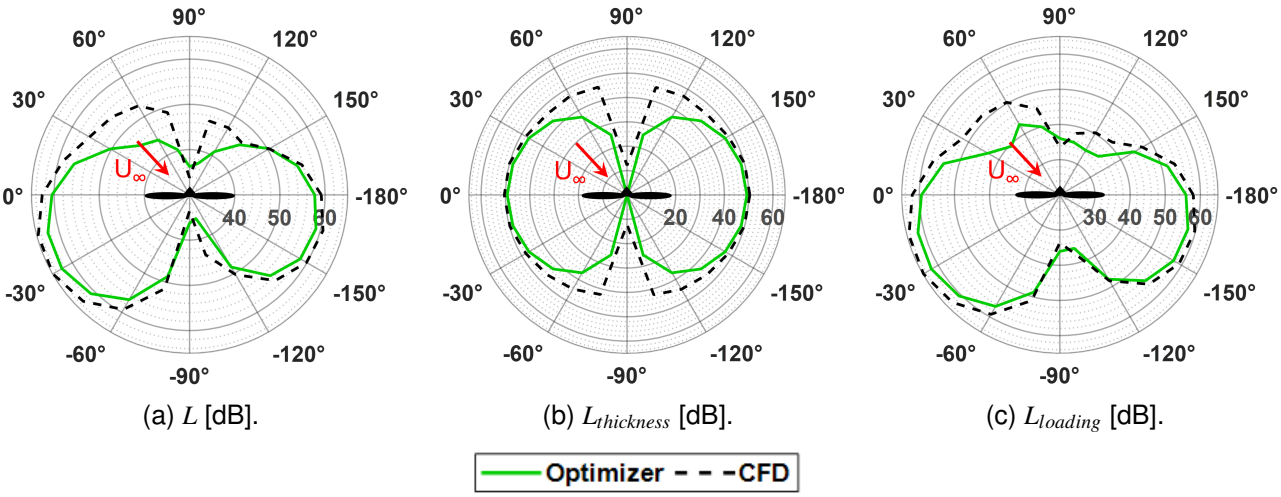
Figure 9 – Comparison of noise spectra in selected emission directions obtained via optimizer and CFD.

To examine whether the agreement in spectral characteristics extends to the spatial radiation pattern, Figure 10 compares the directivity of the unweighted sound pressure level $L$ and its individual thickness- and loading-noise contributions. The evaluation is performed in the plane perpendicular to the rotor disk and aligned with the flight direction ($\Psi = 0°/180°$), at a constant observer distance of 30 m. Despite differences in absolute level, the optimizer reproduces the characteristic asymmetric directivity predicted by CFD (Figure 10a). Both methods show the highest levels below the rotor plane, with $L_{max}$ located between $\Phi = -15°$ and $-30°$. Agreement is particularly good across the lower hemisphere, whereas larger deviations occur for observers above the rotor disk.

The separated source contributions provide further insight into these differences. The thickness-noise directivity (Figure 10b) exhibits the expected symmetric radiation pattern, with two distinct lobes showing maximum levels close to the rotor plane and decreasing levels toward the propeller axis. This characteristic shape is reproduced by both methods, with particularly good agreement near the rotor plane. Toward the propeller axis, however, the predictions increasingly diverge. While the BEMT-based solution approaches the theoretically expected vanishing thickness-noise contribution along the propeller axis [13], the CFD-based prediction retains finite levels. This discrepancy is likely tied to numerical differences in how the FW-H equation is evaluated within the respective acoustic solvers. It was found that the CFD-based thickness-noise prediction exhibits unexpected high-frequency content, which has also been reported by [21] and could could contribute to the observed deviations.

In contrast to the approximately symmetric thickness-noise field, the loading-noise directivity (Figure 10c) exhibits a pronounced asymmetry. Both methods predict elevated levels below the rotor plane, with the dominant radiation lobe again centered between $\Phi = -15°$ and $-30°$. The close

agreement in the orientation of this lobe indicates that the BEMT-based framework captures the principal effect of the azimuthally varying blade loading induced by the oblique inflow. Since loading noise dominates the total tonal level, its asymmetric radiation pattern also explains the corresponding shape of the overall directivity. Differences in $L_{\text{loading}}$ magnitude remain, particularly above the rotor disk, where CFD predicts higher levels over several observer angles. These deviations indicate limitations of the reduced-order aerodynamic representation in reproducing the complete unsteady blade loading obtained from CFD. Nevertheless, the dominant radiation direction and the overall asymmetric loading-noise pattern are consistently reproduced by both methods.




(a) $L$ [dB]. (b) $L_{thickness}$ [dB]. (c) $L_{loading}$ [dB].

Figure 10 – Directivity plots within the plane perpendicular to the rotor disk and aligned with the forward flight direction ($\Psi$ = 180 ° / 0 °) comparing optimizer and CFD results.

Finally, the comparison is extended to the A-weighted sound pressure level, which is of particular relevance since $L_{A,\max}$ constitutes the acoustic objective of the optimization. In addition, A-weighting accounts for the frequency-dependent sensitivity of human hearing and is therefore relevant for assessing community noise. Figure 11 compares $L_A$ over the lower receiver hemisphere at a distance of 30 m. Both methods reproduce the general radiation pattern, with the highest levels occurring in the forward-facing sector between approximately $\Psi = 150°$ and $260°$. This agreement is also reflected in the location of $L_{A,\max}$ summarized in Table 2. Although the optimizer underpredicts the maximum level by 5 dB(A), both methods predict a similar emission direction, confirming that the maximum noise levels are radiated within the range of elevation angles identified in Figure 10.

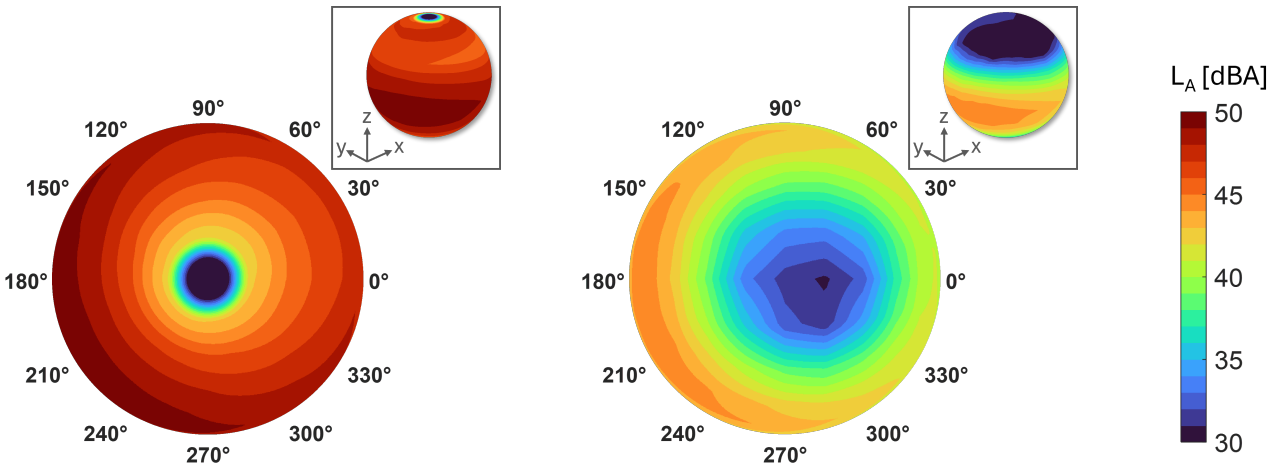
Table 2 – Magnitude and emission angles of $L_{A,\max}$ for the noise optimized design as predicted by the optimizer and the CFD simulation.

| **Method** | $L_{A,\max}$ **[dB(A)]** | $\Psi$ [°] | $\Phi$ [°] |
|---|---|---|---|
| Optimizer | 44.8 | 200 | -24 |
| CFD URANS | 49.8 | 200 | -16 |

Notably, the optimizer-predicted $L_{A,\max}$ reported in Table 2 is higher than the $L_{A,\max} = 42.9$ dB(A) reported for Design 1 on the Pareto front (see Figure 4a). This deviation arises from the limited receiver set used to evaluate the acoustic objective, as defined in Section 2.2. Reconstruction of the complete receiver sphere identifies a higher predicted maximum outside this original receiver set. Thus, the increase from 42.9 to 44.8 dB(A) results from the spatial sampling of the acoustic objective, while the remaining difference to the CFD prediction reflects differences between the two prediction methodologies.

Larger differences between optimizer and CFD are apparent in the low-noise region. While the CFD solution predicts the minimum-$L_A$ region approximately along the propeller axis (see Figure 11a), the optimizer predicts a broader low-noise region that is displaced toward the backward emission

direction ($\Psi = 0°$). The location and extent of this low-level region therefore differ more strongly between the methods than suggested by the previously discussed unweighted directivity. The three-dimensional projections in the upper-right insets of Figure 11 additionally reveal the behavior over the full receiver sphere. While CFD maintains comparatively high A-weighted levels over much of the upper hemisphere, the optimizer predicts substantially lower levels for observers above the rotor disk. The discrepancy in $L_A$ is therefore not restricted to individual observer directions but extends over substantial regions of the radiated sound field.




(a) CFD. (b) Optimizer.

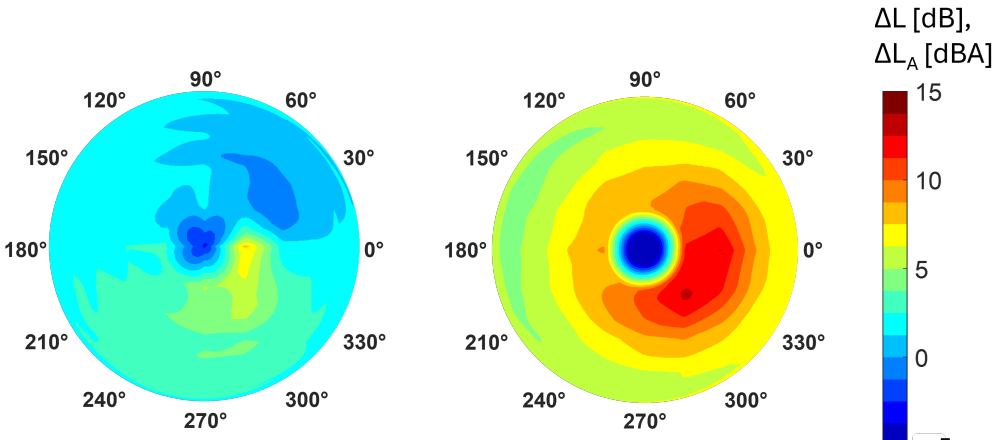
Figure 11 – Top view of the lower noise hemispheres showing the A-weighted sound pressure level, $L_A$, at a radial distance of 30 m from the rotor center (flight direction toward $\Psi$ = 180°). Inset shows a 3D perspective view of the full acoustic field.

A more quantitative view of these differences is provided in Figure 12, which shows $\Delta L = L_{CFD} - L_{Opt}$ and $\Delta L_A = L_{A,CFD} - L_{A,Opt}$ across the lower noise hemisphere. Positive values indicate an underprediction by the optimizer relative to the CFD simulation. For the unweighted level, $\Delta L$ remains within approximately $\pm 5$ dB over the majority of observer locations. In contrast, $\Delta L_A$ is predominantly positive over large parts of the hemisphere, revealing a systematic tendency of the optimizer to underpredict the A-weighted level compared to the CFD simulation. The deviations reach ≈7 dB(A) within the rotor plane and exceed 10 dB(A) in observer regions with high elevation angles aft of the rotor. The substantially different spatial distributions of $\Delta L$ and $\Delta L_A$ demonstrate that the discrepancy cannot be described by a simple constant offset between the two prediction methods.

The substantially larger deviations in $L_A$ compared with the unweighted level $L$ can be traced to the spectral differences identified in Figure 9. The unweighted level is dominated by the strong low-order tonal components, for which both methods show comparatively good agreement. A-weighting strongly attenuates these low-frequency components, thereby increasing the relative contribution of the higher harmonics [22]. Consequently, discrepancies in higher-frequency harmonic content have a considerably greater influence on $L_A$ than on $L$. This effect is particularly apparent in the forward spectrum, where CFD predicts elevated harmonic content around 1 kHz that is not reproduced by the optimizer. The systematic underprediction of $L_A$ therefore primarily reflects differences in spectral content rather than a failure to reproduce the principal radiation direction.

Overall, the CFD comparison supports the use of the BEMT-based framework for identifying aerodynamic and acoustic design trends, as it reproduces the integral propeller performance, dominant tonal components, and principal radiation characteristics with comparatively low computational effort. However, the observed discrepancies in higher-order harmonic content and the resulting systematic underprediction of $L_A$ demonstrate that the framework should not be interpreted as a high-fidelity predictor of absolute A-weighted noise levels. In addition, the difference between the optimization objective and the reconstructed full-sphere $L_{A,\max}$ highlights the importance of sufficient receiver coverage when defining the acoustic objective. The framework is therefore most appropriately used for computationally efficient design-space exploration and comparative acoustic optimization, followed

by higher-fidelity assessment of selected configurations.




(a) $\Delta L$. (b) $\Delta L_A$.

Figure 12 – Top view of the lower noise hemispheres showing the level differences ($\Delta = CFD - BEMT$) in unweighted and A-weighted sound pressure levels ($\Delta L$ and $\Delta L_A$) at an observer radius of 30 m.

## 4. Conclusion

This study investigated the aerodynamic and acoustic mechanisms governing the noise optimization of a hover propeller under a 45° climb condition. The optimization identifies a noise-reduction potential exceeding 5 dB(A) relative to the baseline for a 3.5% reduction in total efficiency. Reduced rotational speed emerges as the main characteristic of the low-noise designs, enabled by adaptations of the blade geometry and sectional operating conditions. Importantly, the acoustic benefit is achieved despite increased aerodynamic loading and without reduced cyclic load variations, demonstrating that conventional aerodynamic unloading is not a prerequisite for low-noise operation. The associated efficiency penalty is primarily electrical rather than aerodynamic, with the motor operating limits ultimately constraining further noise reduction.

The acoustic analysis confirms reductions in both thickness and loading noise, while retaining the characteristic asymmetric directivity associated with the oblique inflow. Comparison with higher-fidelity CFD shows good agreement in integral aerodynamic performance, dominant tonal components, and principal radiation characteristics, but reveals an underprediction of approximately 5 dB(A) in $L_{A,\max}$. Overall, the results demonstrate the suitability of the BEMT-based framework for computationally efficient comparative acoustic optimization, while higher-fidelity methods remain necessary for accurate prediction of absolute noise levels.

## 5. Acknowledgments

This research has been conducted as part of the MuteNet project funded by the State of Bavaria in cooperation with Phoenix-Wings GmbH, manufacturer of the herein investigated vertical take-off and landing cargo drone 'PW.Orca'. Further acknowledgment regarding the computational and data resources is directed to the Leibniz Supercomputing Centre (www.lrz.de).

## 6. Contact Author Email Address

For any questions, please contact: teresa.moses@tum.de

## 7. Copyright Statement

The authors confirm that they, and/or their company or organization, hold copyright on all of the original material included in this paper. The authors also confirm that they have obtained permission, from the copyright holder of any third party material included in this paper, to publish it as part of their paper. The authors confirm that they give permission, or have obtained permission from the copyright holder of this paper, for the publication and distribution of this paper as part of the ICAS proceedings or as individual off-prints from the proceedings.

## References


[1] Raza, W., Renkhoff, J., Ogirimah, O., Bawa, G. K., and Stansbury, R. S., "Advanced Air Mobility: Innovations, Applications, Challenges, and Future Potential," *Journal of Air Transportation*, Vol. 33, No. 2, April 2025, pp. 169–187.

[2] Schmähl, M. and Hornung, M., "Implementation and validation of an optimization-based propeller design program," *CEAS Aeronautical Journal*, May 2025.

[3] Gur, O. and Rosen, A., "Optimization of Propeller Based Propulsion System," *Journal of Aircraft*, Vol. 46, No. 1, Jan. 2009, pp. 95–106.

[4] Moreira, C., Herzog, N., and Breitsamter, C., "Wind Tunnel Investigation of Transient Propeller Loads for Non-Axial Inflow Conditions," *Aerospace*, Vol. 11, No. 4, March 2024, pp. 274.

[5] Phoenix Wings GmbH, "https://phoenixwings.com/pworca/," Online, March 2026.

[6] Baerens, T., Schmahl, M., and Hornung, M., "Noise Modeling of a Tilt-Rotor Air Taxi Configuration Utilizing a Hybrid Acoustic Analogy Approach," *Proceedings of the Vertical Flight Society 80th Annual Forum*, The Vertical Flight Society, May 2024, pp. 1–17.

[7] Thiele, M., Obster, M., and Hornung, M., "Aerodynamic Modeling of Coaxial Counter-Rotating UAV Propellers," 2019.

[8] Leishman, J. G., *Principles of helicopter aerodynamics*, No. 18 in Cambridge aerospace series, Cambridge University Press, Cambridge [u.a.], 2nd ed., 2006.

[9] Brentner, K. S. and Farassat, F., "Modeling aerodynamically generated sound of helicopter rotors," *Progress in Aerospace Sciences*, Vol. 39, No. 2–3, Feb. 2003, pp. 83–120.

[10] Farassat, F., "Derivation of Formulations 1 and 1A of Farassat," techreport 20070010579, Langley Research Center, Hampton, Virginia, 2007.

[11] Ffowcs Williams, J. E. and Hawkings, D. L., "Sound Generation by Turbulence and Surfaces in Arbitrary Motion," *Philosophical Transactions of the Royal Society of London. Series A, Mathematical and Physical Sciences*, Vol. 264, No. 1151, 1969, pp. 321–342.

[12] Padula, S. L. and Block, P. J. W., "Predicted changes in advanced turboprop noise with shaft angle of attack," *Journal of Propulsion and Power*, Vol. 1, No. 5, 1985, pp. 381–387.

[13] Goyal, J., Sinnige, T., Ferreira, C., and Avallone, F., "Effect of Angle of Attack on Propeller Aeroacoustics at Positive and Negative Thrust," *Journal of Aircraft*, Vol. 62, No. 5, 2025, pp. 1130–1150.

[14] "ISO 2533:1975, Standard Atmosphere," 1975.

[15] Curl, N., "The influence of solid boundaries upon aerodynamic sound," *Proceedings of the Royal Society of London. Series A. Mathematical and Physical Sciences*, Vol. 231, No. 1187, Sept. 1955, pp. 505–514.

[16] Regier, A. A. and Hubbard, H. H., "Status of Research on Propeller Noise and Its Reduction," *The Journal of the Acoustical Society of America*, Vol. 25, No. 3, May 1953, pp. 395–404.

[17] Ismail, K. A. R. and Rosolen, C. V. A. G., "Effects of the airfoil section, the chord and pitch distributions on the aerodynamic performance of the propeller," *Journal of the Brazilian Society of Mechanical Sciences and Engineering*, Vol. 41, No. 3, Feb. 2019.

[18] Chirico, G., Barakos, G. N., and Bown, N., "Numerical aeroacoustic analysis of propeller designs," *The Aeronautical Journal*, Vol. 122, No. 1248, Nov. 2017, pp. 283–315.

[19] Hubbard, H., Lansing, D., and Runyan, H., "A review of rotating blade noise technology," *Journal of Sound and Vibration*, Vol. 19, No. 3, 1971, pp. 227–249.

[20] Rizzi, S. A., Huff, D. L., Boyed, D. D., Bent, P., Henderson, B. S., Pascioni, K. A., Sargent, D. C., Josephson, D. L., Marsan, M., He, H., and Snider, R., "Urban Air Mobility Noise: Current Practice, Gaps, and Recommendations," techreport 20205007433, Langley Research Center, Hampton, Virgina, Oct. 2020.

[21] Schmähl, M. and Hornung, M., "Optimization of propellers under consideration of aeroacoustic and aerodynamic goals and installation effects," *186th Meeting of the Acoustical Society of America and the Canadian Acoustical Association*, Vol. 54, ASA, 2024, p. 040010.

[22] Little, D. S., Majdalani, J., Hartfield, R. J., and Ahuja, V., "On the prediction of noise generated by urban air mobility (UAM) vehicles. I. Integration of fundamental acoustic metrics," *Physics of Fluids*, Vol. 34, No. 11, Nov. 2022.